Effect of Truncated Projections on Defect Detection in Attenuation-Compensated Fanbeam Cardiac SPECT

George K. Gregoriou, Benjamin M.W. Tsui and Grant T. Gullberg
Departments of Biomedical Engineering and Radiology, The University of North Carolina at Chapel Hill, Chapel Hill, North Carolina at Chapel Hill; and Department of Radiology, University of Utah, Salt Lake City, Utah

For some camera systems used in cardiac SPECT, the limited field of view of fanbeam-collimated detectors produces truncation in the projection data. This truncation may generate artifacts and distortions in the transmission CT images and in the attenuation-corrected myocardial SPECT images (that use the transmission CT images as attenuation maps), thus affecting clinical diagnosis. Concern over this problem stimulated us to evaluate the effect of truncation with human observer performance studies. **Methods:** A three-dimensional mathematical cardiac-torso phantom that realistically models the attenuation and ^{201}Tl uptake distributions in different organs of the upper torso was used for the investigation. Five degrees of truncation (from 0% to 40% truncation) in the projection data were simulated by the use of five different detector sizes collimated by fanbeam collimators. The attenuation maps were obtained by reconstructing the truncated transmission data generated from these fanbeam geometries. The emission data obtained with the same fanbeam geometries were reconstructed by using the maximum likelihood-expectation maximization algorithm and were corrected for attenuation using the reconstructed attenuation maps. Two observer performance studies were performed. In Study 1, the images were reconstructed without using the body contour as support, whereas in Study 2, the exact body contour was used in reconstructing both the attenuation maps and the attenuation-corrected SPECT images. **Results:** The results of the receiver operating characteristics analysis indicate that there is very little difference between detection for the various degrees of truncation, and this difference only becomes noticeable for severe truncation of greater than 40%. **Conclusion:** Using the acquisition and processing methods, we found the use of the body contour as support in reconstructing truncated transmission CT and SPECT data reduces the loss of defect detectability in attenuation-compensated myocardial SPECT images due to truncated data.

Key Words: fanbeam myocardial SPECT; truncated projection; observer performance study; receiver operating characteristics study

J Nucl Med 1998; 39:166–175

The wide acceptance from the SPECT imaging community of the necessity for compensating for photon attenuation (*1–10*) has made it necessary to modify existing SPECT systems to allow for transmission CT (TCT). Recently, three-detector SPECT systems have been upgraded to allow acquisition of both transmission and emission data so that the reconstructed transmission map can be used to correct for photon attenuation in the SPECT images (*5–7*). The three detectors with fanbeam collimators are arranged with a transmission line source at the focal line of one of the detectors. Transmission and emission data are acquired in one detector while the other two simultaneously acquire emission data. The detectors are positioned carefully in a triangular arrangement so that the incident transmission flux from the line source is not truncated by detectors adjacent to the line source. Although the fanbeam geometry results in an increase in sensitivity and/or spatial resolution for brain imaging (*11,12*), the limited field of view (FOV) of the fanbeam-collimated detector makes it difficult to acquire the fanbeam TCT and SPECT data of the thorax without truncating the projections in most of the views.

Images reconstructed from truncated projection data display various artifacts and distortions. In the case of the filtered backprojection (FBP) method (*13–15*), these artifacts appear in the form of a hot ring at the truncation edge, and the pixel values outside the untruncated region are very small. In the case of iterative methods, such as the maximum likelihood–expectation maximization (ML-EM) algorithm (*16,17*) and the weighted least squares–conjugate gradient algorithm (*18,19*), the artifact appears in the form of a cold ring at the truncation edge, and the values outside the untruncated region are nonzero (*14*). In iterative reconstruction methods, if information about the body contour is used in choosing the support, the truncation artifacts are reduced (*14,15*). However, the effect of such artifacts on defect detectability in terms of sensitivity and specificity of human observers has not been investigated. Although some studies have compared parallel-beam to converging-beam geometries in terms of myocardial defect detection (*20,21*), the effect of truncation caused by such converging beam geometries was not considered.

The effect of truncated projections in fanbeam myocardial SPECT was investigated by observer performance studies and receiver operating characteristics (ROC) analysis. Realistic transmission and emission projection data with and without myocardial defects were simulated by using a mathematical phantom. Five degrees of truncation in the projection data were simulated by changing the detector size. The truncated TCT and SPECT data were reconstructed using the ML-EM algorithm (*16,17*) with attenuation compensation, with and without the body contour as support in the image reconstructions. Two observer studies were conducted using five classes of images representing five degrees of truncation. Study 1 was performed without support, and Study 2 was performed with support. The results from the observer performance studies were analyzed using the ROC method to evaluate the effect of truncation in reconstructing the attenuation maps and the SPECT images on myocardial defect detection.

MATERIALS AND METHODS

Three-Dimensional Mathematical Cardiac-Torso Phantom

The three-dimensional mathematical cardiac-torso (MCAT) phantom is a mathematical description that realistically models the anatomy and the activity uptake distribution of different organs in the upper human torso (*22*). The phantom is quite versatile and

Received Jul. 10, 1996; revision accepted Mar. 16, 1997.
For correspondence or reprints contact: Benjamin M. W. Tsui, PhD, CB 7575, 152 MacNider Hall, University of North Carolina, Chapel Hill, NC 27599.

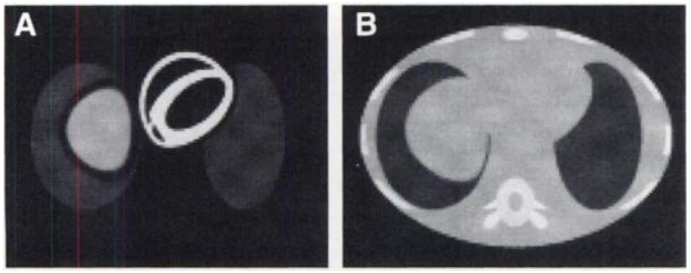

FIGURE 1. A sample transaxial slice through the MCAT phantom at the level of the heart. (A) Thallium-201 uptake distribution. (B) Attenuation coefficient distribution for 75-keV photons in different tissues.

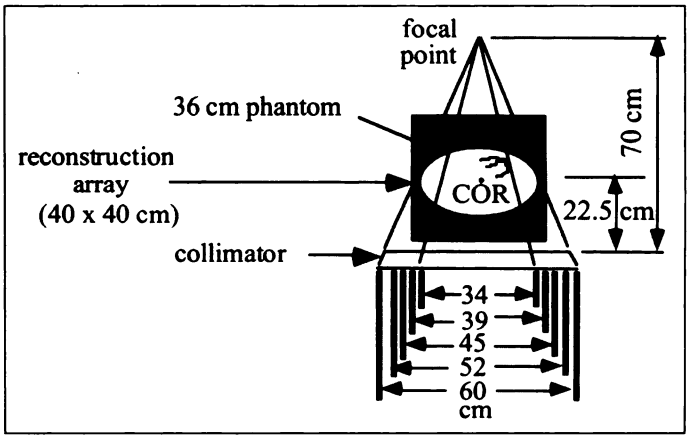

FIGURE 2. The fanbeam geometry used in our study. The focal length of the fanbeam collimator is 70 cm. The phantom has a lateral width of 36 cm. The COR is at the center of the phantom, and the radius of rotation is 22.5 cm. Five different sizes of detector were used in the study, giving different degrees of truncation. They are 60 cm (0% truncation), 52 cm (11.8% truncation), 45 cm (22.5% truncation), 39 cm (31.8% truncation) and 34 cm (40.1% truncation).

flexible. It permits, among other things, the modeling of different patient sizes, various shapes and compositions of female breasts, rib cage, walls and chambers of the cardiac ventricles, apical thinning of the myocardium, raised liver dome, stomach and one or two arms, if desired. Furthermore, the MCAT phantom allows for the simulation of activity uptake from various radionuclide agents and for the simulation of attenuation distributions corresponding to either monoenergetic or polyenergetic (spectrum) sources.

For this myocardial SPECT study, the relative concentrations of ^{201}Tl in the heart, kidneys, liver, spleen, lungs and soft tissues were assumed to be 0.043, 0.036, 0.019, 0.012, 0.006 and 0.002, respectively. Similarly, the linear attenuation coefficients of the cortical bones, trabecular bones, lungs and muscle at 72 keV, which is the average energy of the photon emissions of ^{201}Tl, were taken to be 0.305, 0.237, 0.056 and 0.187 cm^{-1}, respectively (*23*). Both the ^{201}Tl activity distribution and the linear attenuation coefficients were digitized into 128 × 128 × 128 matrices with 3.1 × 3.1 × 3.1 mm^3 voxels. A sampled transaxial slice through the thorax of the MCAT phantom with 36-cm lateral width used in the study corresponding to ^{201}Tl uptake and attenuation distribution is shown in Figure 1.

Myocardial defects modeled as three-dimensional Gaussian-shaped decreases in the uptake of myocardial activity were simulated. The defect size characterized by the FWHM of the Gaussian was set at 1.5 cm. The defect contrast was adjusted by varying the amplitude of the Gaussian distribution.

In placing the myocardial defects, a similar methodology as that reported in earlier articles (*20*) was followed to avoid cross-talk, due to partial volume effects, between defects in adjacent slices. Four transaxial slices through the heart of the MCAT phantom and spaced 12.5 mm apart were selected for the study. In each slice, a total of eight possible sites that allow placement of myocardial defects were chosen avoiding the area where the ventricular walls meet and the boundary between the atria and the ventricles. Eight phantoms were used. Each contained a defect placed at one of the defect sites in each of the four selected slices. No defect was placed directly above or below another.

Multiple defects on each phantom were used to increase the efficiency of data generation. Each of the eight phantoms had a different set of defects so that all 32 possible defect sites on the four slices were used. A phantom with no defects was also generated to simulate a defect-free situation.

Simulation of Transmission CT and Emission CT Projection Data

Emission projection data were simulated including the effects of photon attenuation, three-dimensional, spatially varying geometric response of the collimator/detector, photon scatter and Poisson noise. A low-energy, high-resolution fanbeam collimator was used, which had a spatial resolution of 14 mm at 25 cm from its face and a focal length of 70 cm. A scintillation camera with 4-mm intrinsic resolution was simulated. The center of rotation (COR) was at 22.5 cm, and the focal point was 70 cm from the collimator face (Fig. 2). The fanbeam collimation resulted in a magnification of 1.6 for an object placed at the COR. Two approaches could be used to generate projection data with different degrees of truncation by changing the size of the collimator/detector or by changing the size of the patients. We chose the first method to keep the size of the myocardium constant in the transaxial slices shown to the observers and, thus, avoid any bias on the part of the observers toward viewing a specific class of image size.

Five degrees of truncation were simulated using camera detector sizes of 60, 52, 45, 39 and 34 cm (Fig. 2). As shown in Figure 2, the FOVs at the center of rotation (COR) with the fanbeam geometry for these detector sizes were 38.0, 32.9, 28.5, 24.7 and 21.5 cm, respectively. The corresponding fractions of the MCAT phantom with 36-cm lateral body width that were truncated by the FOVs were 0%, 11.8%, 22.5%, 31.8% and 40.1%, respectively. If the same degrees of truncation had been simulated by increasing patient size instead, for a 40-cm camera and the same geometry used in the study (i.e., radius of rotation of 22.5 cm and focal length of 70 cm), the patients would have had lateral body widths of 24.0, 27.7, 32.0, 36.9 and 42.4 cm, respectively. By considering the range of sizes of patients undergoing SPECT scans, one can see that the first two sizes are much less than normal size, but the last three are quite commonly found in clinical myocardial studies.

The large 60-cm detector was chosen so that there would be no truncation for a patient with 36-cm body width when the fanbeam geometry is used. With the 34-cm detector there was severe truncation of the surrounding organs but not of the myocardium. The projections of the myocardium were not truncated in any of the projection views in general. In one projection, the edge of the projection view touched the tip of the myocardium. The projection bin size for all five detector sizes was 3.1 mm, which resulted in 192, 168, 144, 126 and 110 bins with nonzero projection values, respectively. A total of 128 projection views over 360° were simulated.

To increase the efficiency of data generation, the simulations were accomplished in several steps. Separate projection data of the myocardium without the defects, the Gaussian-shaped defects alone and the other organs in the torso were obtained (*20*) including the effects of attenuation and collimator/detector response. The projection data obtained from the defects and the heart were then appropriately weighted and combined. The effect of scatter was incorporated by convolving each of the two-dimensional projection views with a scatter response function. The scatter response

function was calculated separately for the heart and for the torso at the water-equivalent depth of the center of mass for the heart and the torso (*20*), respectively. The projection datasets from the heart and the torso were then combined and scaled so that the total number of counts overall projection views in a 6.1-mm slice resembled clinically obtained counts of about 172,000 for a 60-cm detector. For the 34-cm detector, the number of counts was about 129,000. For the rest of the detector sizes, the number of counts lay between 172,000 and 129,000. Finally, to simulate experimentally obtained data, Poisson noise was added to the projections. For each of the eight phantoms that included defects in four separate slices, two noisy projection datasets were generated. Thus, a total of 16 projection datasets were simulated with defects. Similarly, 16 noisy projection sets were obtained from the defect-free phantom.

To obtain areas under the ROC curves in the desirable range of 0.75–0.85 (*24*), we conducted a series of preliminary observer studies using a small set of test images. The contrast value of the myocardial defects (defined as the difference between the activity uptake in the myocardium and the defect, divided by the uptake in the myocardium) was changed iteratively until the area under the ROC curve obtained from the observer study fell within the "desirable range" of 0.75–0.85. The contrast value of 0.8 gave an area under the ROC that fell within this range. This contrast was chosen to be used in the study.

The transmission projection data were synthesized assuming the same fanbeam geometry as that used for the emission data. The simulated data were noise-free and had perfect resolution. Angular samples of 128 angles were obtained over 360° with a bin size of 3.1 mm for all five detector sizes.

Reconstruction of Attenuation Maps and SPECT Images

A comparison of quantitative accuracy of attenuation maps reconstructed from the TCT data for the five degrees of truncation was made using the FBP algorithm, the transmission ML-EM algorithm (*16-17*) without the body contour as support and the transmission ML-EM algorithm using the exact body contour as support. The ML-EM algorithm was chosen for the comparison rather than the weighted least squares–conjugate gradient because it gave quantitatively better reconstructions due to its inherent positivity constraint on the reconstructed pixel values. The TCT images or attenuation maps were reconstructed in 128 × 128 matrices using the transmission ML-EM algorithm with 60 iterations.

To evaluate the quantitative accuracy of the attenuation maps obtained from the three reconstruction techniques described, the attenuation factors used in the SPECT image reconstructions with attenuation compensation were calculated. For each projection view, the attenuation factor for a specific pixel is the negative exponential of the integral of the attenuation coefficients from that pixel to the detector along a ray passing through the pixel, i.e.:

$$IM_\theta(r) = \exp\left(-\int_r^\infty ds\mu(r')\right). \qquad \text{Eq. 1}$$

Figure 3 shows a schematic diagram of computing the attenuation factor of pixel r for projection angle θ. If this is calculated for all pixels in the array, an image of attenuation factors results. This image is called an integral map (IM). Pixel values in the IMs are an alternative representation of the reconstructed attenuation map evaluated at projection angle θ. They depict the attenuation factors actually used in the projector/backprojection operations in the iterative attenuation compensation technique (*25*).

One way to evaluate the effect of truncation on the quantitative accuracy of the attenuation maps obtained from the three reconstruction techniques is to compare profiles through the IMs for the truncated reconstructions with that obtained for the true phantom. Also, the root mean square error (RMSE) between individual IMs

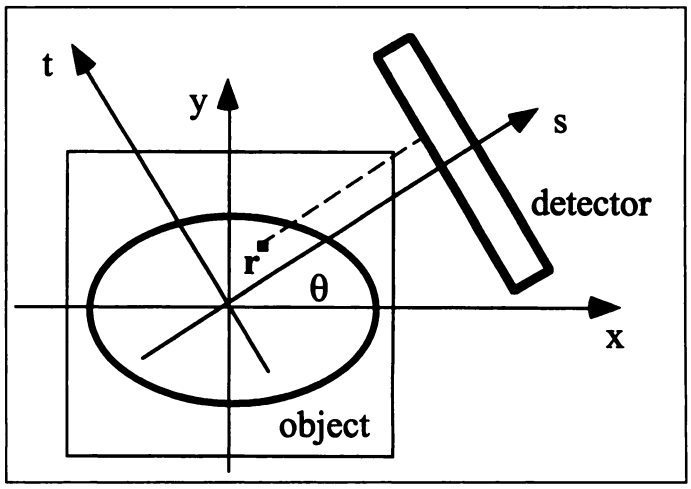

FIGURE 3. The attenuation factor for pixel r at projection angle θ is obtained by computing the negative exponential of the integral of attenuation coefficients along a line perpendicular to the detector, which originates at r and terminates at the detector. The IM for projection angle θ is obtained by displaying the attenuation factors obtained for each pixel in the form of a two-dimensional image.

and the IM of the phantom (over several angles) can be used for the evaluation. The RMSE was calculated inside the elliptic body contour of the phantom using:

$$RMSE = \sqrt{\frac{1}{nm}\sum_{i=1}^{m}\sum_{j\in ROI}\left(\frac{IM_i(j) - IM_i^p(j)}{IM_i^p(j)}\right)^2}, \qquad \text{Eq. 2}$$

where ROI is the region of interest (region inside the body contour), n is the number of pixels in the ROI, m is the number of angles for which the IMs were computed, IM_i is the IM (corresponding to the ith projection angle) obtained from the reconstructed image to be evaluated and IM_i^p is the IM obtained from the phantom.

The SPECT images (four slices from each dataset or phantom) were reconstructed with 60 iterations of the ML-EM algorithm using attenuation compensation with and without the body contour as support. The number of iterations chosen was based on a subjective evaluation of the reconstructed images that show the best image quality with compromise between image resolution (improves with number of iterations) and noise (increases with number of iterations).

No compensation for the collimator/detector response or scatter was performed. The 32 projection datasets (16 with and 16 without defects) for each of the five detector sizes were reconstructed, producing five classes of images. For each study, 4 slices from each of the 16 datasets with defects and 4 from each of the 16 sets without defects provided a total of 128 noisy reconstructed images for each class. Furthermore, for each study, the noise-free projection data (eight with defects and one without) were reconstructed and used for training the observers.

The reconstructed SPECT images were postfiltered with a two-dimensional Butterworth filter (rather than a three-dimensional because only four slices were reconstructed from each projection dataset, and they were not adjacent) of order 8 and a cutoff frequency of 0.4 cycles/cm. The degree of smoothing is close to that commonly used in clinical myocardial SPECT. After filtering, all negative pixel values were set to zero (as is commonly done in clinical practice), normalized and converted to displayed intensities. For each group of images, the maximum pixel value of each image in the group was determined. The 10th percentile of all the maximum values was chosen as the group's maximum pixel value (*20*). Any pixel value between zero and the group's maxi-

mum pixel value was linearly mapped into the displayed intensity range of 0–247 (the range of 248–255 was reserved for graphics). Pixel values higher than the group's maximum pixel value were set to 247; this way, the effect of exceptionally high values due to extraneous image noise was reduced. The images were subsequently extrapolated to 256 × 256 pixels for display. After image extrapolation, the displayed images occupied approximately 8 × 8 cm^2 on the display monitor. Each reconstructed image from the same class and the same image slice was assigned to a group.

Observer Performance Experiments and Receiver Operating Characteristics Analysis

For the two observer performance experiments, the observers were shown transaxial reconstructed image slices from the five classes obtained with the different detector sizes corresponding to different degrees of truncation. Half the images contained a myocardial defect, and half were defect-free. The task of the observer was to indicate his/her confidence in detecting a defect at a specified location indicated by a cross-hair cursor. The observer sessions were performed in a darkened room. The images and graphics were displayed against a black background. The entire image display on the monitor was divided into four areas (*20*). One area was used for displaying the image to be evaluated. The second was used for placing the continuous scale marked by five confidence categories: definitely absent, probably absent, possibly present, probably present and definitely present. After removing the cross-hair by clicking a button, the observer indicated his/her confidence about the presence of a defect by the position selected on the scale. This rating could be changed by reselecting a new position. The third area was used for communication between the observer and the computer. Finally, the last area was used only for the training sessions.

A subset of 32 images of the 128 from each class was used for training the observers. The remaining 96 images were split into two smaller blocks of 48 each for the observer study. This split was necessary to show different blocks of images from different classes in a different sequence to each observer, thus eliminating any reading order effect (*24*). The observer viewing session consisted of two parts. During the first, a set of 16 training images from each class was shown to the observer to familiarize him/her with the characteristics of the images and the experimental procedure (*24*). After the observers had indicated the certainty with which they detected a defect at a specified location, the noise-free reconstructed image corresponding to that slice was presented, and the truth about the presence or absence of a defect was revealed. The second part of the experiment (after training) was the actual observer performance study. The blocks of images from the different classes and the ordering of images within each block were randomized for each observer. A smaller training set consisting of eight images was shown before each test block of images.

Six observers participated in the observer performance study. The observers could view the images from any comfortable distance and were given unrestricted amounts of time to complete the test. On average, two studies were performed in two 45-min sessions on 2 consecutive days for each observer. In each study, 640 images were evaluated. Study 1 had the attenuation-corrected images obtained by using the attenuation map reconstructed without support. Study 2 had the images obtained by using the body contour as support.

For the ROC analysis (*24,26*) of the experimentally obtained data, the software package developed by Metz et al. (*27*) was used. This program groups the continuous rating scores into discrete categories represented by specific false-positive fractions and true-positive fractions. Because false-positive and true-positive fractions are linearly related in the normal deviate coordinates, the data are fitted to a straight line by using the maximum likelihood method. An ROC curve is specified by the y-intercept A and the slope B of the fitted straight line. Statistical tests were performed to evaluate the differences between the ROC curves obtained from the observer performance experiments.

The area (A_z) under the ROC curves was used for comparing the five classes of images in each study. The null hypothesis (H_0) that the areas (A_z) under two ROC curves were the same was tested against the alternative hypothesis (H_a) that they were different. Specifically, a two-tailed paired Student's t-test was used in the hypothesis testing. The average areas (A_z) for each class of images were calculated from all six observers, which resulted in five degrees of freedom for the Student's t-test. The Student's t-test was applied pairwise on the five different classes of images, i.e., a total of 10 comparisons were performed per study. The p values associated with each possible comparison were also calculated, together with the 95% confidence intervals about the differences. Finally, an interstudy statistical analysis was performed on pairs of classes formed by comparing a certain class from Study 1 to the corresponding class in Study 2 to test any significant difference in the performance of the two studies.

RESULTS

The attenuation maps obtained from the reconstruction of TCT data, together with profiles through the myocardium, are shown in Figures 4, 5 and 6 for the FBP algorithm, the transmission ML-EM algorithm without support and the transmission ML-EM algorithm with support, respectively. Also included are the corresponding profiles through the IMs, calculated from the attenuation maps using Equation 1, with the detector at the anterior side of the patient. In each figure, the phantom is shown (for comparison) with the TCT-reconstructed attenuation maps corresponding to the 60-, 52-, 45-, 39- and 34-cm detectors.

Figure 4 shows results from the FBP-reconstructed attenuation maps. The presence of a hot ring artifact is evident especially for higher degrees of truncation. The ring appears immediately inside the truncation edge, and the values of the image pixels outside the ring are very small. The pixel values in the middle of the reconstructed images vary from lower to higher than that of the phantom as the degree of truncation increases from 0% to 40%. Figure 4C shows that the IM from the FBP-reconstructed TCT images deviates from that of the phantom.

Figure 5 shows results from the transmission ML-EM-reconstructed images in which no support was used in the reconstruction. The reconstructed images have nonzero values outside the body contour. A cold ring artifact is present where the truncation edge occurs. The reconstructed attenuation maps, within the truncation edge, show smaller differences whereas more severe artifacts are shown outside the edge as compared to the known phantom. The attenuation coefficient values within the truncation edge deviate more from the true values as the degree of truncation increases. Outside the truncation edge, they extend at some positive value to the end of the image array. Figure 5C shows that, although the attenuation map images in Figure 5 are significantly distorted, the attenuation factors (or pixel values of the IM) have fairly good accuracy within the truncation edge. A similar observation was made in a review paper on convergent-beam tomography (*14*).

Figure 6 shows the effect of imposing the body contour with the ML-EM reconstructions. In this case, all pixels outside the body contour are forced to be zero, and as a consequence, the magnitude of the ring artifact is reduced. Furthermore, in the

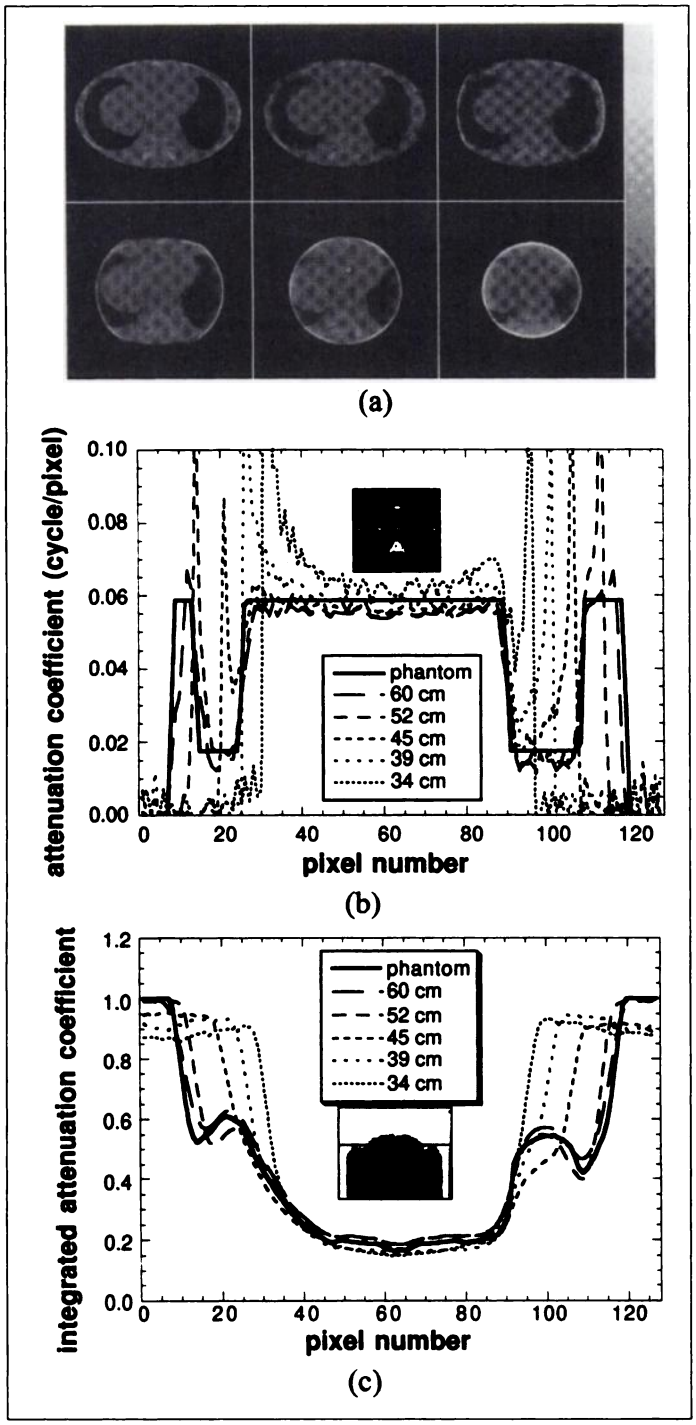

FIGURE 4. (A) Reconstructed attenuation maps obtained by using the FBP algorithm through the same transaxial slice. From top left to bottom right are the attenuation maps from the phantom and from using the 60-, 52-, 45-, 39- and 34-cm detectors. (B) Horizontal profiles from the attenuation maps shown in A, at the level of the heart, as indicated. (C) Horizontal profiles from the IMs at the same level of the heart as in B. An example of the IMs is also shown.

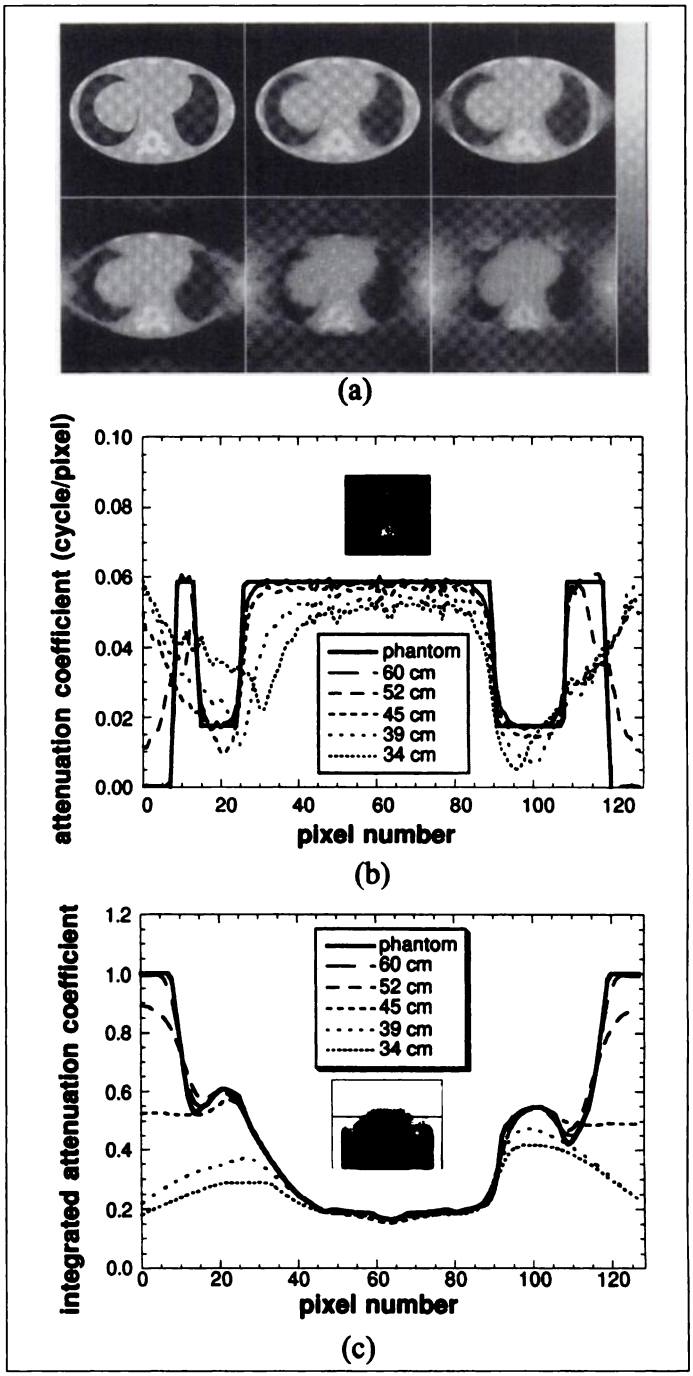

FIGURE 5. (A) Reconstructed attenuation maps obtained by using the ML-EM algorithm without the body contour as support and with 60 iterations. From top left to bottom right are the attenuation maps from the phantom and from using the 60-, 52-, 45-, 39- and 34-cm detectors. (B) Horizontal profiles from the attenuation maps shown in A, at the level of the heart, as indicated. (C) Horizontal profiles from the IMs at the same level of the heart as in B. An example of the IMs is also shown.

fully sampled (untruncated) area that includes the location of the myocardium, the profiles from the attenuation maps obtained from the different degrees of truncation follow closely the profile of the phantom. In Figure 6C, the IMs show the least amount of difference between the degrees of truncation indicating a smaller dependence of the reconstructed attenuation maps on the degree of truncation. On the other hand, Figure 4C displays the greatest differences between the degrees of truncation, especially outside the ring artifact, which indicates a higher sensitivity to truncation of the FBP-reconstructed TCT images.

Figure 7 shows the RMSE for the individual IMs corresponding to the different reconstruction methods as a function of degree of truncation. Note that, in the absence of truncation, the RMSE values of all three methods are close to zero and show the least amount of difference. The FBP method was the most sensitive to the degree of truncation, whereas the ML-EM algorithm produces better quality attenuation maps than does the FBP and allows for including a priori information about the body contour in the reconstructions of attenuation maps and

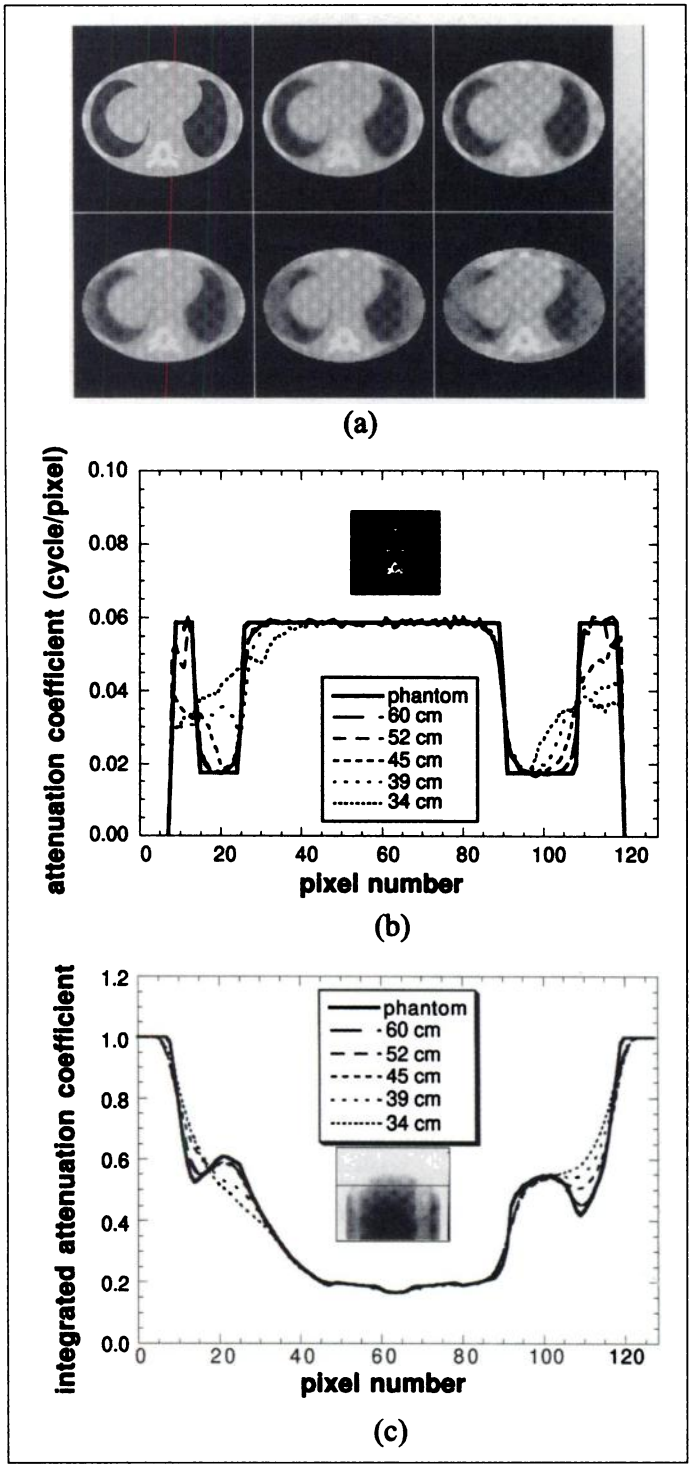

FIGURE 6. (A) Reconstructed attenuation maps obtained by using the ML-EM algorithm with the body contour as support and with 60 iterations. From top left to bottom right are the attenuation maps from the phantom and from using the 60-, 52-, 45-, 39- and 34-cm detectors. (B) Horizontal profiles from the attenuation maps shown in A, at the level of the heart, as indicated. (C) Horizontal profiles from the IMs at the same level of the heart as in B. An example of the IMs is also shown.

attenuation-compensated SPECT images. The RMSE increases with decrease in detector size (increase in the degree of truncation) with the maps obtained from the 34-cm detector, displaying the largest RMSE in all cases. The FBP has the largest RMSE. Between the two ML-EM-based methods, the one that uses the exact body contour as support displays the smallest dependence on the degree of truncation.

Figures 8 and 9 show noise-free SPECT images reconstructed

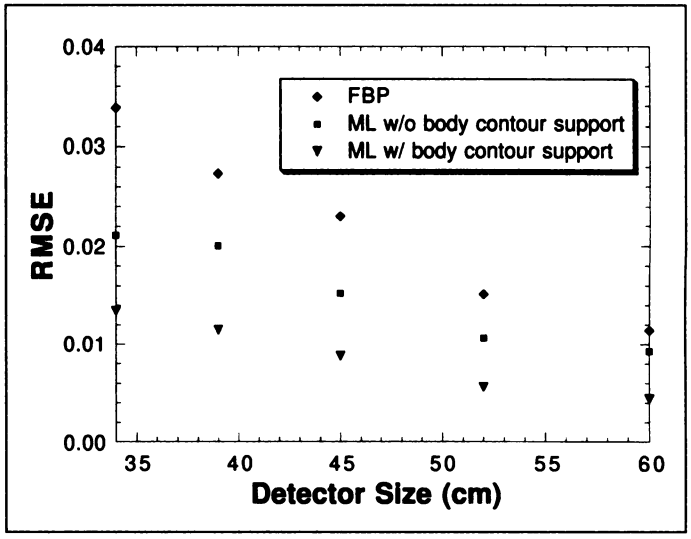

FIGURE 7. The RMSE of the IMs obtained from TCT images, reconstructed using different algorithms and different detector sizes with respect to that of the phantom. The RMSE is calculated over all pixels inside the body contour.

by using 60 iterations of the ML-EM algorithm with attenuation compensation. In Figure 8, both the SPECT images and the attenuation maps were reconstructed without using the body

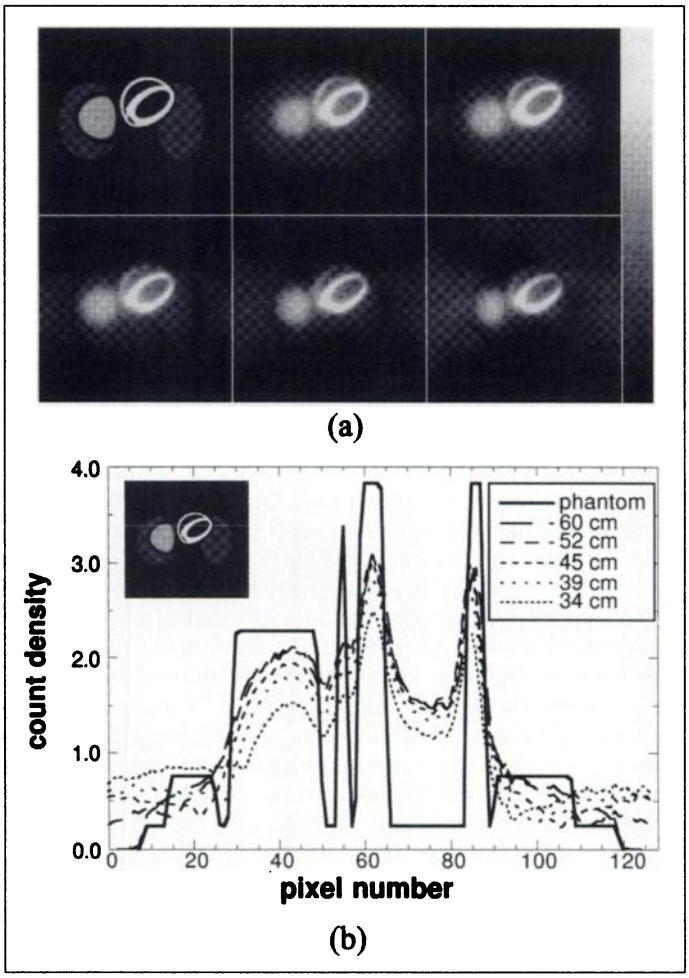

FIGURE 8. (A) SPECT images reconstructed using 60 iterations of the ML-EM algorithm with attenuation compensation, without the body contour as support. From top left to bottom right are images from the phantom and from using the TCT and SPECT data from the 60-, 52-, 45-, 39- and 34-cm detectors. (B) Horizontal profiles from the SPECT images shown in A, at the level of the heart, as indicated.

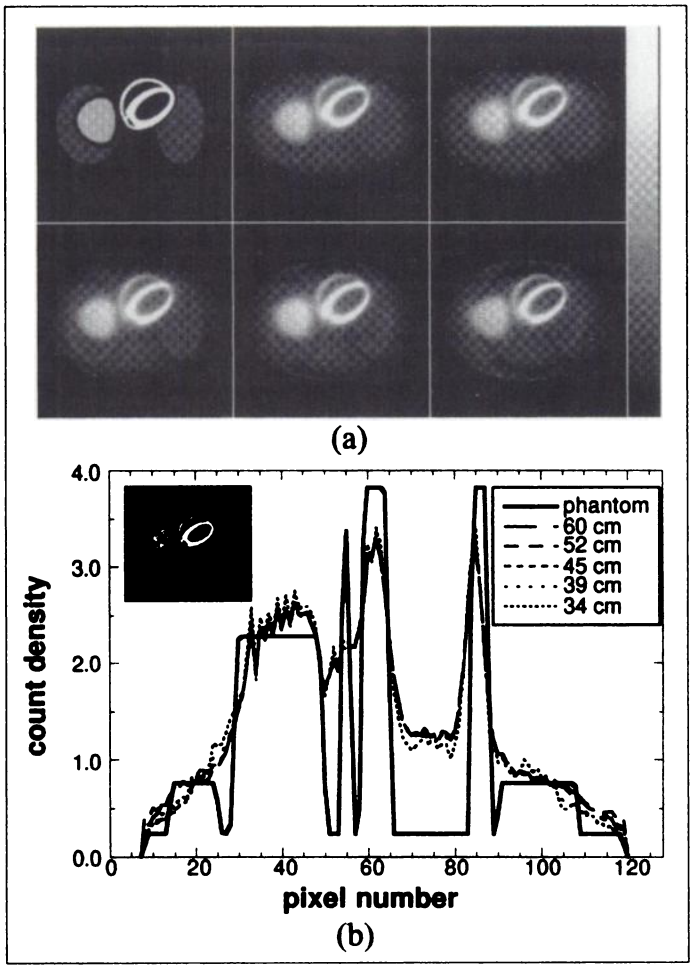

FIGURE 9. (A) SPECT images reconstructed using 60 iterations of the ML-EM algorithm with attenuation compensation, with the body contour as support. From top left to bottom right are images from the phantom and from using the TCT and SPECT data from the 60-, 52-, 45-, 39- and 34-cm detectors. (B) Horizontal profiles from the SPECT images shown in A, at the level of the heart, as indicated.

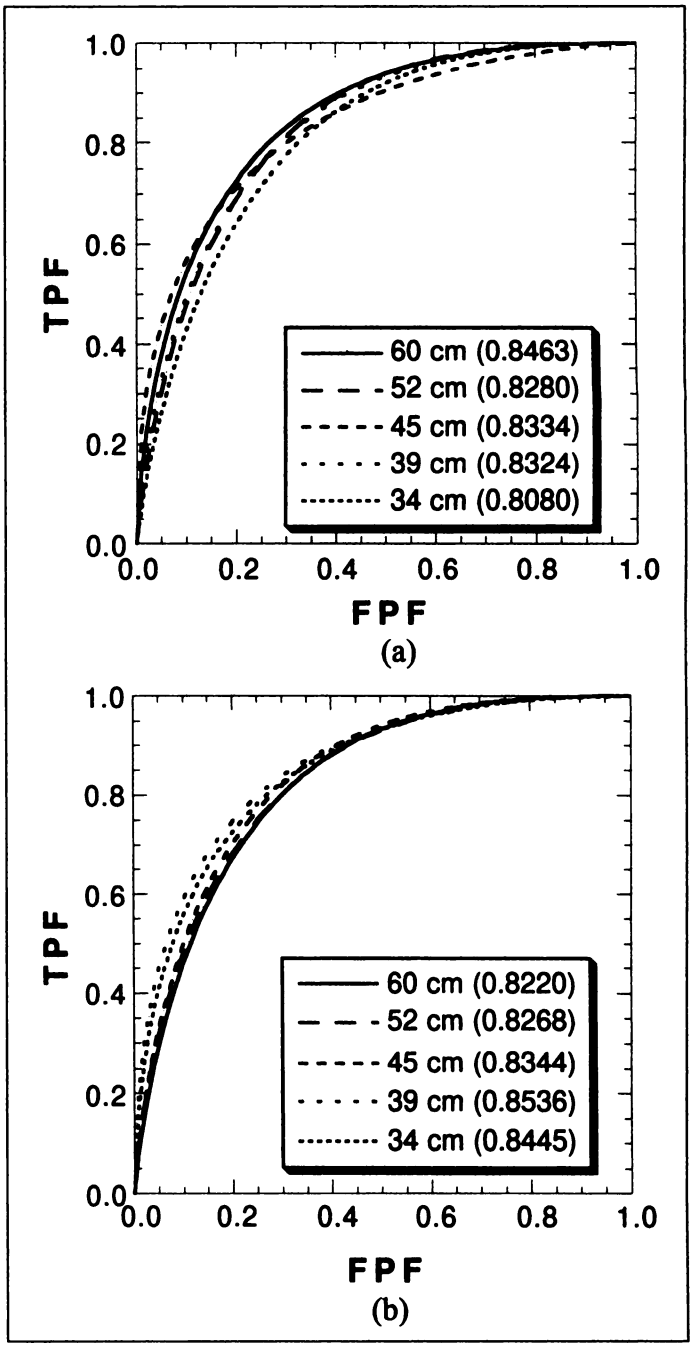

FIGURE 10. Average ROC curves from six observers obtained from the 60-, 52-, 45-, 39- and 34-cm detectors. (A) Results from Study 1 (ML-EM-reconstructed TCT images without support). (B) Results from Study 2 (ML-EM-reconstructed TCT images using body contour as support). The areas under the ROC curves are shown in parentheses.

contour as the support, whereas in Figure 9, the exact body contour was used as the support. The main difference between these two results is the presence of activity distribution outside the body contour in the images reconstructed without support (Figure 8) and the presence of a cold ring artifact (similar to that of the reconstructed attenuation maps) in both figures, which is more dramatic without support (Figure 8), especially for higher degrees of truncation. As can be seen from the profiles, the reconstructed activity distribution varies with the degree of truncation without support (Figure 8), but this variation lessens with support (Figure 9). More importantly, the profiles obtained with support show higher image contrast in the myocardium than that obtained without support. It should be noted that, in both figures, the reconstructed myocardial uptake distribution is lower than that of the phantom because of blurring due to the collimator/detector response function and the photon scatter, both of which are not compensated for in the reconstructions.

The results of the observer performance experiments are shown in Figure 10 and Tables 1–5. Figure 10A shows the average ROC curves for the five classes of images obtained from Study 1 (without support). Figure 10B shows the results of Study 2 (with support). Tables 1 and 2 list the areas (A_z) under the ROC curves of individual observers for each class of images (corresponding to different degrees of truncation) in Study 1 and Study 2, respectively. Also shown are the average areas (A_z) among the observers and the associated s.d. Figure 10A and Table 1 suggest that, without support, the average defect detectability is virtually unaffected by the different degrees of truncation except in the case of severe truncation, i.e., the 34-cm detector size. On the other hand, Figure 10b and Table 2 suggest an improvement in defect detectability for the case with severe degree of truncation if body contour is used as support information. This improvement can be attributed to the increase in image contrast as observed in the image profiles shown in Figures 8 and 9.

Tables 3 and 4 show a two-tailed Student's t-test statistical analysis on the average difference in the area under the ROC curves for pairs of classes of images in Study 1 and Study 2, respectively. Also shown are the corresponding p values and the

TABLE 1
Area under the ROC Curves from Individual Observers (A_z): Study 1*

Detector size (cm)	Individual A_z						Average A_z	s.d.
	Observer 1	Observer 2	Observer 3	Observer 4	Observer 5	Observer 6		
60	0.8621	0.8319	0.8121	0.8287	0.8742	0.8685	0.8463	0.0253
52	0.8491	0.8112	0.8216	0.7908	0.8932	0.8023	0.8280	0.0376
45	0.8752	0.8655	0.8018	0.7922	0.8460	0.8196	0.8334	0.0341
39	0.8506	0.8588	0.8501	0.7865	0.8144	0.8338	0.8324	0.0275
34	0.8035	0.8302	0.8117	0.8099	0.8430	0.7494	0.8080	0.0322

*Images were reconstructed without body contour as support.

95% confidence intervals of the average difference. The Student's t-test was performed on all 10 possible combinations of classes in each study. The analysis indicates that, in Study 1 (without support) and at a significance level of 0.1, the defect detectability in the 34-cm detector class of images is lower than that of all other classes of images (Table 3). All the other comparisons indicate no significant difference except for the comparison of 60-cm to 50-cm detector size. In Study 2 (with support), the analysis indicates that, in general, there is no significant difference of myocardial defect detection among all detector sizes except between the image classes corresponding to the detector sizes of 60 cm and 39 cm.

Finally, Table 5 shows a two-tailed Student's t-test analysis for each class of images between the two studies. This analysis shows that, at a significance level of 0.1, the reconstruction method used in Study 2 performed better in the presence of severe truncation. Specifically, the use of the body contour improved the defect detectability in the cases of the 34- and 39-cm detectors. The differences in detectability between the 60-cm detector (with 0% truncation) in the two studies can be attributed to statistical fluctuations in the data and is an area that requires further studies. The results of the analysis indicate that the FBP-reconstructed attenuation maps are, by far, the worst, with the highest RMSE. Between the two ML-EM techniques, the one that uses exact support produces the best results, with the lowest RMSE.

DISCUSSION

In this study, an interesting result was noted when the 60-cm detector was simulated. The area under the ROC curve was greater without support than it was with support. This result may be attributed to a few factors. First, the initial image estimates used in the reconstruction are different. When no support was used, the initial image estimate was a uniform image spanning the entire reconstructed image matrix. When support is used, the initial image estimate was a uniform image

TABLE 2
Area under the ROC Curves from Individual Observers (A_z): Study 2*

Detector size (cm)	Individual A_z						Average A_z	s.d.
	Observer 1	Observer 2	Observer 3	Observer 4	Observer 5	Observer 6		
60	0.8140	0.7876	0.8495	0.8228	0.8661	0.7919	0.8220	0.0312
52	0.7849	0.8494	0.8481	0.8588	0.8115	0.8082	0.8268	0.0294
45	0.8221	0.8190	0.8943	0.8744	0.7839	0.8127	0.8344	0.0415
39	0.8785	0.8267	0.8560	0.8680	0.8470	0.8456	0.8536	0.0182
34	0.8639	0.7959	0.8377	0.8482	0.8430	0.8781	0.8445	0.0280

*Images were reconstructed with body contour as support.

TABLE 3
Two-Tailed Paired Student's t-Test Statistical Analysis: Study 1*

Pair of detector sizes used in comparison (cm)	Average difference in A_z	s.d. of the difference	t statistic (5 df)	p value (5 df)	95% confidence interval
60/52	0.0182	0.0312	1.4288	0.0986	(−0.0145, 0.0509)
60/45	0.0129	0.0514	1.0035	0.1793	(−0.0201, 0.0459)
60/39	0.0139	0.0393	0.8663	0.2086	(−0.0273, 0.0552)
60/34	0.0383	0.0450	2.0825	0.0410	(−0.0089, 0.0855)
52/45	−0.0054	0.0357	−0.3669	0.3637	(−0.0429, 0.0321)
52/39	−0.0043	0.0451	−0.2351	>0.4000	(−0.0516, 0.0430)
52/34	0.0201	0.0341	1.4442	0.0970	(−0.0157, 0.0559)
45/39	0.0010	0.0290	0.0858	>0.4000	(−0.0294, 0.0314)
45/34	0.0254	0.0396	1.5719	0.0837	(−0.0162, 0.0670)
39/34	0.0244	0.0434	1.4416	0.0972	(−0.0212, 0.0700)

df = degrees of freedom.
*Images were reconstructed without body contour used as support.

TABLE 4
Two-Tailed Paired Student's t-Test Statistical Analysis: Study 2*

Pair of detector sizes used in comparison (cm)	Average difference in A_z	s.d. of the difference	t statistic (5 df)	p value (5 df)	95% confidence interval
60/52	−0.0048	0.0426	−0.2780	>0.4000	(−0.0495, 0.0399)
60/45	−0.0124	0.0490	−0.6212	>0.4000	(−0.0638, 0.0390)
60/39	−0.0316	0.0317	−2.4485	0.0610	(−0.0649, 0.0017)
60/34	−0.0225	0.0407	−1.3538	0.2365	(−0.0652, 0.0202)
52/45	−0.0076	0.0320	−0.5803	>0.4000	(−0.0412, 0.0260)
52/39	−0.0268	0.0394	−1.6666	0.1654	(−0.0682, 0.0146)
52/34	−0.0176	0.0516	−0.8372	0.4366	(−0.0718, 0.0366)
45/39	−0.0192	0.0390	−1.2090	0.2783	(−0.0601, 0.0217)
45/34	−0.0101	0.0516	−0.4775	>0.4000	(−0.0643, 0.0441)
39/34	0.0092	0.0222	1.0129	0.3531	(−0.0141, 0.0325)

df = degrees of freedom.
*Images were reconstructed with body contour used as support.

spanning only the support region. Second, results from a recent study (*28*) show that the convergence rates of the iterative reconstruction algorithm are faster with support, resulting in both higher image contrast and higher image noise than those without support. Careful examination of the profiles through the emission images in Figures 9 and 10 show similar phenomena. This may imply that the image quality of the attenuation-compensated images critically depends on the number of iterations and on whether support is used in image reconstruction. The ROC results may be indicating that, at 60 iterations, the noise dominates any gain in contrast with support.

Did the results of the study reflect deterministic or statistical changes as a function of truncation? In human observer studies, the results of the ROC study correlate with the image noise levels and the lesion contrast. However, based on the results of a previous study, it is anticipated that the statistical fluctuations for the different degrees of truncation were virtually the same (*29*). Therefore, it would appear that, in this study, detection was more affected by myocardial defect contrast changes as a function of truncation. Analysis of the profiles shows that, as the truncation increases, the myocardium to ventricle contrast decreases whereas, with support, the contrast remains nearly the same for all degrees of truncation except for the 39- and 34-cm detectors. Inferring that the defect contrast is related to the myocardium to ventricle contrast, the plots indicate that, in these cases, the defect contrast also increased, which would explain the improved area under the ROC curves for these two cases. It appears that, as truncation approaches the heart, the truncation ring artificially improves the contrast in the cardiac region. This is evident from the profile plots of the attenuation-corrected emission images.

In performing a study such as this, there is always the question of how well the results correlate with clinical diagnostic practices. Significant effort was expended to make the computer-generated heart phantom realistic, which included simulation of liver, lungs, bone and soft tissues (*22*). The physics of the imaging process in clinical acquisitions was duplicated by including attenuation, scatter and geometric point response of the SPECT imaging system in the simulations. However, the study used only simple Gaussian-shaped myocardial defects. The task of the observers involved simple detection, a situation in which he/she was asked to look at an identified location and to give a numerical ranking of his/her confidence that the myocardial defect was present. The simulated myocardial defect shape was not necessarily what one would expect to see from an occlusion of a coronary artery. Physicians also do not look at one area identified by a cursor but, instead, look at several slices of the heart and incorporate other information into their decision process such as electrocardiogram results, patient symptoms and, in some cases, an angiogram.

Despite these limitations in this study, it is anticipated that these results will extrapolate to clinical diagnosis. Receiver operating characteristic observer studies are a well-recognized methodology for evaluating imaging systems and methodology or, as in this case, the effects of imperfect data. A single three-dimensional phantom modeling the cardiac torso of a standard patient was used to simulate the large amounts of data

TABLE 5
Two-Tailed Paired t-Test Statistical Analysis Between Studies 1 and 2

Pair of detector sizes used in comparison (cm)	Average difference in A_z	s.d. of the difference	t statistic (5 df)	p value (5 df)	95% confidence interval
60/60	0.0243	0.0403	1.4759	0.0502	(−0.0180, 0.0666)
52/52	0.0012	0.0593	0.0502	>0.4000	(−0.0524, 0.0634)
45/45	−0.0010	0.0696	−0.0358	>0.4000	(−0.0830, 0.0721)
39/39	−0.0213	0.0373	−1.3948	0.0939	(−0.0605, 0.0179)
34/34	−0.0365	0.0557	−1.6049	0.0802	(−0.0950, 0.0220)

df = degrees of freedom.

needed for a ROC study. Although the phantom does not simulate the heterogeneity of tissue within organs and normal variations in patient anatomy and radioactivity distributions, it provides a realistic simulation of the anatomy of an average patient to compare the different degrees of truncation.

The results are encouraging and point to the potential of using transmission and emission data acquired from a three-detector SPECT system for improving myocardial defect detection and the diagnosis of ischemia of the coronary blood vessels over that of conventional cardiac SPECT. This ROC study indicates that reconstruction inaccuracies due to truncation will not significantly affect the diagnostic accuracy of attenuation cardiac SPECT except perhaps in those cases of very large patients. Although these results are encouraging, we recognize that a clinical study is, by far, the best way to establish the definitive improvement in clinical specificity and sensitivity of attenuation-corrected cardiac SPECT.

CONCLUSION

The effect of projection truncation on defect detection in attenuation corrected fanbeam cardiac SPECT images was studied with no reconstruction support and with the exact body contour as the support. Realistic truncated projection data that included the effects of photon attenuation, three-dimensional collimator/detector response, scatter and noise were simulated using the three-dimensional MCAT phantom. Five degrees of truncation, ranging from no truncation to severe truncation of 40%, were simulated by changing the detector size. Two observer performance studies were performed with images reconstructed by the ML-EM algorithm, with and without the body contour as the support. The results of these studies showed that, when the body contour is used as the support in reconstruction of both the attenuation maps and the SPECT images, the defect detectability in images generated with excessive truncation is reduced.

The results indicate that, in general, there is very little difference between detection for the various degrees of truncation chosen for the study. This difference is not significant, considering the statistical fluctuations in the results. It becomes noticeable only for the severe truncation of 40%. When the body contour information was used as support, the differences were reduced. Also, with or without support, the reconstructed attenuation coefficient values and values of the integrated maps obtained from the ML-EM algorithm varied very little within the cardiac region as a function of truncation. Truncation had little effect on the emission image quality in the cardiac region. A better estimate of the emission intensity was obtained with support. However, both with and without support, the emission intensity varied little with the degree of truncation except for the case with most severe truncation without support in the myocardial region.

ACKNOWLEDGMENTS

This work was partially supported by U. S. Public Health Grants HL39792 and CA39463. We thank Dawn Tavares for the careful reading of the manuscript.

REFERENCES

1. Malko JA, Van Heertum RL, Gullberg GT, Kowalsky WP. SPECT liver imaging using an iterative attenuation correction algorithm and an external flood source. *J Nucl Med* 1986;27:701–705.
2. Bailey DL, Hutton BF, Walker PJ. Improved SPECT using simultaneous emission and transmission tomography. *J Nucl Med* 1987;28:844–851.
3. Tsui BMW, Gullberg GT, Edgerton ER, et al. Correction of nonuniform attenuation in cardiac SPECT imaging. *J Nucl Med* 1989;30:497–507.
4. Frey EC, Tsui BMW, Perry JR. Simultaneous acquisition of emission and transmission data for improved thallium-201 cardiac SPECT imaging using a technetium-99m transmission source. *J Nucl Med* 1992;33:2238–2245.
5. Tung C-H, Gullberg GT, Zeng GL, Christian PE, Datz FL, Morgan HT. Nonuniform attenuation correction using simultaneous transmission and emission converging tomography. *IEEE Trans Nucl Sci* 1992;39:1134–1143.
6. Manglos SH, Bassano DA, Thomas FD, Grossman ZD. Imaging of the human torso using cone beam transmission CT implemented on a rotating gamma camera. *J Nucl Med* 1992;33:150–156.
7. Jaszczak RJ, Gilland DR, Hansen MW, Jang S, Greer KL, Coleman RE. Fast transmission CT for determining attenuation maps using a calibrated line source, rotatable air-copper-lead attenuators and fanbeam collimation. *J Nucl Med* 1993;34:1577–1586.
8. Tan P, Bailey DL, Meikle SR, Eberl S, Fulton RR, Hutton BF. A scanning line source for simultaneous emission and transmission measurements in SPECT. *J Nucl Med* 1993;34:1752–1760.
9. Ficaro EP, Fessler JA, Rogers WL, Schwaiger M. Comparison of americium-241 and technetium-99m as transmission sources for attenuation correction of thallium-201 SPECT imaging of the heart. *J Nucl Med* 1994;35:652–663.
10. Kemp BJ, Prato FS, Nicholson RL, Reese L. Transmission computed tomography imaging of the head with a SPECT system and a collimated line source. *J Nucl Med* 1995;36:328–335.
11. Jaszczak RJ, Chang LT, Murphy PH. Single photon emission computed tomography using multi-slice fan beam collimators. *IEEE Trans Nucl Sci* 1979;26:610–618.
12. Tsui BMW, Gullberg GT, Edgerton ER, Gilland DR, Perry JR, McCartney WH. Design and clinical utility of a fan beam collimator for SPECT imaging of the head. *J Nucl Med* 1986;27:810–819.
13. Chang LT. Attenuation correction and incomplete projection in single photon emission computed tomography. *IEEE Trans Nucl Sci* 1979;26:2780–2789.
14. Gullberg GT, Zeng GL, Datz FL, Christian PE, Tung CH, Morgan HT. Review of convergent beam tomography in single photon emission computed tomography. *Phys Med Biol* 1992;37:507–534.
15. Manglos SH. Truncation artifact suppression in cone-beam radionuclide transmission CT using maximum likelihood techniques: evaluation with human subjects. *Phys Med Biol* 1992;37:549–562.
16. Lange K, Carson R. EM reconstruction algorithms for emission and transmission tomography. *J Comput Assist Tomogr* 1984;8:306–316.
17. Lange K, Bahn M, Little R. A theoretical study of some maximum likelihood algorithms for emission and transmission tomography. *IEEE Trans Med Imaging* 1987;6:106–114.
18. Huesman RH, Gullberg GT, Greenberg WL, Budinger TF. *Donner algorithms for reconstruction tomography*, RECLBL library users manual. Berkeley, CA: Lawrence Berkeley Laboratory, University of California; 1977.
19. Tsui BMW, Zhao XD, Frey EC, Gullberg GT. Comparison between ML-EM and WLS-CG algorithms for SPECT image reconstruction. *IEEE Trans Nucl Sci* 1991;38:1766–1772.
20. Tsui BMW, Terry JA, Gullberg GT. Evaluation of cardiac cone-beam single photon computed tomography using observer performance experiments and receiver operating characteristic analysis. *Invest Radiol* 1993;28:1101–1112.
21. Li J, Jaszczak RJ, Turkington TG, et al. An evaluation of lesion detectability with cone-beam, fanbeam and parallel-beam collimation in SPECT by continuous ROC study. *J Nucl Med* 1994;35:135–140.
22. Tsui BMW, Zhao XD, Gregoriou GK, et al. Quantitative cardiac SPECT reconstruction with reduced image degradation due to patient anatomy. *IEEE Trans Nucl Sci* 1991;41:2838–2844.
23. Bradley-Moore PR, Lebowitz E, Greene MW, Atkins HL, Ansari AN. Thallium-201 for medical use. II: Biologic behavior. *J Nucl Med* 1975;16:156–160.
24. Metz CE. Some practical issues of experimental design and data analysis in radiological ROC studies. *Invest Radiol* 1989;24:234–245.
25. Gullberg GT, Huesman RH, Malko JA, Pelc NJ, Budinger TF. An attenuated projector-backprojector for iterative SPECT reconstruction. *Phys Med Biol* 1985;30:799–816.
26. Metz CE. ROC methodology in radiologic imaging. *Invest Radiol* 1986;21:720–733.
27. Metz CE, Herman BA, Shen J-H. Maximum-likelihood estimation of ROC curves from continuously-distributed data. *Statistics in Medicine*. In press: 1998.
28. Tsui BMW, Lewis DP, Frey EC, Lalush DS. Reconstruction of truncated TCT and SPECT data from a right-angle dual-camera system for myocardial SPECT. In: *Conference record of the 1996 IEEE Nuclear Science Symposium and Medical Imaging Conference*. Piscataway, NJ: IEEE, Inc.; 1997:1643–1647.
29. Tung C-H. Nonuniform attenuation correction in cardiac SPECT using simultaneous transmission and emission converging tomography [PhD thesis]. Salt Lake City: University of Utah; 1994.